MIT Libraries | DSpace@MIT

MIT Open Access Articles

H[subscript 2]-assisted CO[subscript 2] thermochemical reduction on La[subscript 0.9]Ca[subscript 0.1]FeO[subscript 3-#] membranes: a kinetics study

The MIT Faculty has made this article openly available. ***Please share*** how this access benefits you. Your story matters.

Citation: Wu, Xiao-Yu, and Ahmed F. Ghoniem. "H[subscript 2]-assisted CO[subscript 2] thermochemical reduction on La[subscript 0.9]Ca[subscript 0.1]FeO[subscript 3-δ] membranes: a kinetics study." ChemSusChem (November 2017) © 2017 WILEY-VCH

As Published: http://dx.doi.org/10.1002/cssc.201701372

Publisher: Wiley Blackwell

Persistent URL: http://hdl.handle.net/1721.1/112311

Version: Author's final manuscript: final author's manuscript post peer review, without publisher's formatting or copy editing

Terms of use: Creative Commons Attribution-Noncommercial-Share Alike

Massachusetts Institute of Technology

H_2-assisted CO_2 thermochemical reduction on $La_{0.9}Ca_{0.1}FeO_{3-\delta}$ membranes: a kinetics study

Dr. Xiao-Yu Wu *, Prof. Ahmed F. Ghoniem

Department of Mechanical Engineering, Massachusetts Institute of Technology, 77 Massachusetts Avenue, Cambridge, MA 02139, USA

Email address: xywu@mit.edu (X.Y. Wu), ghoniem@mit.edu (A.F. Ghoniem)

Abstract

Kinetics data for CO_2 thermochemical reduction in an isothermal membrane reactor is required to identify the rate-limiting steps. Here, we report a detailed reaction kinetics study on this process supported by an $La_{0.9}Ca_{0.1}FeO_{3-\delta}$ (LCF-91) membrane. The dependence of CO_2 reduction rate on various operating conditions is examined such as CO_2 concentration on the feed side, fuel concentrations on the sweep side and temperatures. CO_2 reduction rate is proportional to the oxygen flux across the membrane, and the measured maximum fluxes are 0.191 and 0.164 μmol cm^{-2} s^{-1} with 9.5% H_2 and 11.6% CO on the sweep side at 990^{o}C, respectively. Fuel is used to maintain the chemical potential gradient across the membrane and CO is used by construction to derive the surface reaction kinetics. This membrane also exhibits stable performances for 106 hours. A resistance-network model is developed to describe the oxygen transport process and the kinetics data are parameterized using the experimental values. The model shows a transition of the rate limiting step between the surface reactions on the feed side and the sweep side depending on the operating conditions.

Key words:

Oxygen permeable membrane, LCF perovskite, H_2-assisted CO_2 reduction, chemical kinetics

1. Introduction

The concentration of greenhouse gas (mainly CO_2 and CH_4) in the atmosphere keeps rising. The global average atmospheric CO_2 concentration is currently above 400 ppm [1]. Capturing and utilizing CO_2 have both environmental and economic benefits [2-5]. As CO_2 is an abundant and cheap C1 feedstock for industry applications [3, 6], upgrading CO_2 to value-added chemicals such as CO [7-9], CH_3OH [10] and CH_4 [11, 12] is an essential step towards a low carbon economy. Recently, CO_2 thermal reduction into CO and O_2 was achieved in a ceria membrane reactor at 1500^{o}C [13]. In this paper, we focus on a fuel-assisted CO_2 thermochemical reduction process on an oxygen permeable membrane (OPM), which operates at a lower temperature range of 850 – 1030^{o}C. When the overall reaction is endothermic, these thermochemical processes can also be an energy storage technology to convert waste or renewable thermal energy into chemical energy [13, 14].

Thermochemical (redox) cycles have been studied to reduce CO_2 using oxygen carriers such as CeO_2 [15], Zn/ZnO [16] and doped $LaMnO_3$ [17]. These cycles usually operates at different oxidation and reduction temperatures [15]. The temperature-swing operation leads to lower efficiency and is harder to be implemented than isothermal processes [18, 19]. Isothermal redox systems, hence, have also been developed to overcome these disadvantages [19-22]. Moreover, CO_2 splitting in an isothermal oxygen permeable membrane reactor that operates at temperature as high as 1500^{o}C was proposed in the 1980s [23] and recently achieved on a ceria membrane [13]. Compared with thermochemical cycles, this membrane reactor has some advantages, e.g., isothermal operation and process intensification into a single reactor unit. In a membrane reactor, CO_2 reduction rates can be accelerated by the heterogeneous reactions and its thermodynamic equilibrium shifted to further dissociate the reactants thanks to in situ product separation. No

electricity is consumed in this thermochemical process. Only carbon-free heat sources from solar or nuclear power is utilized to reduce CO_2.

Oxygen permeable membranes (OPM) that operate at intermediate temperatures 700 – 1000^{o}C have been the subject of several studies [24]. The formation of stable carbonates makes barium (Ba) containing membranes less than optimal for a CO_2 reduction process. An oxygen flux as high as 1.58 μmol cm^{-2} s^{-1} was reported in the literature on a 1.0 mm thick Nb_2O_5-doped $SrCo0.4Fe_{0.5}Zr_{0.1}O_{3-\delta}$ (SCFZ) perovskite membrane with CO_2 feed and CH_4 sweep at 900^{o}C [25]. Different porous layers with catalysts were coated on both sides (i.e., a mixture of $La_{0.8}Sr_{0.2}MnO_{3-\delta}$–yttria stabilized zirconia-Pd on the CO_2 feed side, and $Sr_{0.7}Ba_{0.3}Fe_{0.9}Mo_{0.1}O_{3-\delta}$-Ni on the CH_4 sweep side) to avoid strontium carbonate formation and stabilize the membrane performance for 500 hours. Another $La_{0.6}Sr_{0.4}Co_{0.2}Fe_{0.8}O_{3-\delta}$ (LSCF) membrane was proposed to decrease carbonate formation tendency and the oxygen flux on this 0.6 mm thick tubular membrane was as high as 0.14 μmol cm^{-2} s^{-1} at 1030^{o}C with CH_4 in the sweep gas [26]. Other type of materials, i.e., dual-phase materials was also tested in the literature. One example is the short-circuit samarium-doped ceria (SDC) membrane with Ag or Pt pastes at the membrane edge [27]. For this ~20 μm thick membrane with Pt catalyst on the CO_2 feed side and SDC/Ag porous support-GdNi/Al_2O_3 catalysts on the CH_4-Ar sweep side, the oxygen flux reported was as high as 0.8 μmol cm^{-2} s^{-1} at 900 ^{o}C [27].

Examining the surface reaction kinetics and the oxygen transport process can help identify the limiting steps and facilitate the development of this CO_2 thermochemical reduction technology. Flux models have been developed for oxygen separation and water splitting on an oxygen permeable membrane [28-30]. This work is one of the first attempts to model CO_2 thermochemical reduction supported by an isothermal membrane reactor, and the results

successfully describe the trends observed in the experiments and shows directions for flux improvement. In this work, we experimentally study the reaction kinetics of CO_2 on a $La_{0.9}Ca_{0.1}FeO_{3-\delta}$ (LCF-91) membrane at temperatures between 850-1030^oC. Based on the experimental data, we develop a resistance-network model to describe the oxygen transport process. This model can be extended to other more complicated membrane configurations, i.e., asymmetric porous supported thin film membranes. LCF-91 perovskite is chosen as it has been tested for air separation and water splitting with stable performances [29-31]. Moreover, carbonate formation is less likely, as calcium carbonate will readily decompose in pure CO_2 environment at atmospheric pressure and above 850^oC [32]. We added either CO or H_2 in the sweep gas to maintain the oxygen partial pressure gradient across the membrane and to study the oxygen transport process. CO is used, by construction, to derive the kinetic parameters for CO_2 thermochemical reduction, while other fuels (i.e., H_2 or hydrocarbons) can be used in practice on the sweep side to reduce the oxygen partial pressure on that side. The effect of the feed and sweep gas species and their concentrations is investigated and the dependence of oxygen flux on these factors is reported and discussed. The resistance-network model, developed based on the experimental data, shows that the surface kinetics of both sides are the rate limiting steps depending on the gas species concentrations and operating temperatures.

2. CO_2 thermochemical reduction on an OPM

2.1 Schematic

A schematic of CO_2 thermochemical reduction on an oxygen permeable membrane is shown in Figure 1. Three processes occur in the vicinity of and across the membrane: (1) carbon dioxide is thermochemically reduced on the oxygen vacancy on the feed side surface into lattice

oxygen and carbon monoxide, while the metal cation is oxidized, (2) lattice oxygen diffuses across the bulk of the membrane, together with the electrons/holes to maintain electronic neutrality in the bulk of the membrane [33], (3) lattice oxygen leaves the sweep side surface as gases or is consumed by fuel oxidation, and the metal cation is reduced. Elevated temperatures raise the rates of these processes and favor CO_2 thermolysis. Oxidation and reduction of the membrane surfaces take place on the feed and sweep side, respectively. Depending on the gases on the sweep side, the overall process may be autothermal, endothermic or exothermic. For example, if CO is used on the sweep side (as done in this study in order to determine the kinetics rate), the overall process is autothermal. If the sweep gases are non-reactive, the overall process is endothermic. In case of CH_4 or H_2 sweep, the overall process is endothermic methane dry reforming or reverse water gas shift, respectively. When the overall reaction is endothermic, heat sources such as concentrated solar or nuclear heat can be utilized to achieve the operating temperatures and supply heat for the reactions.

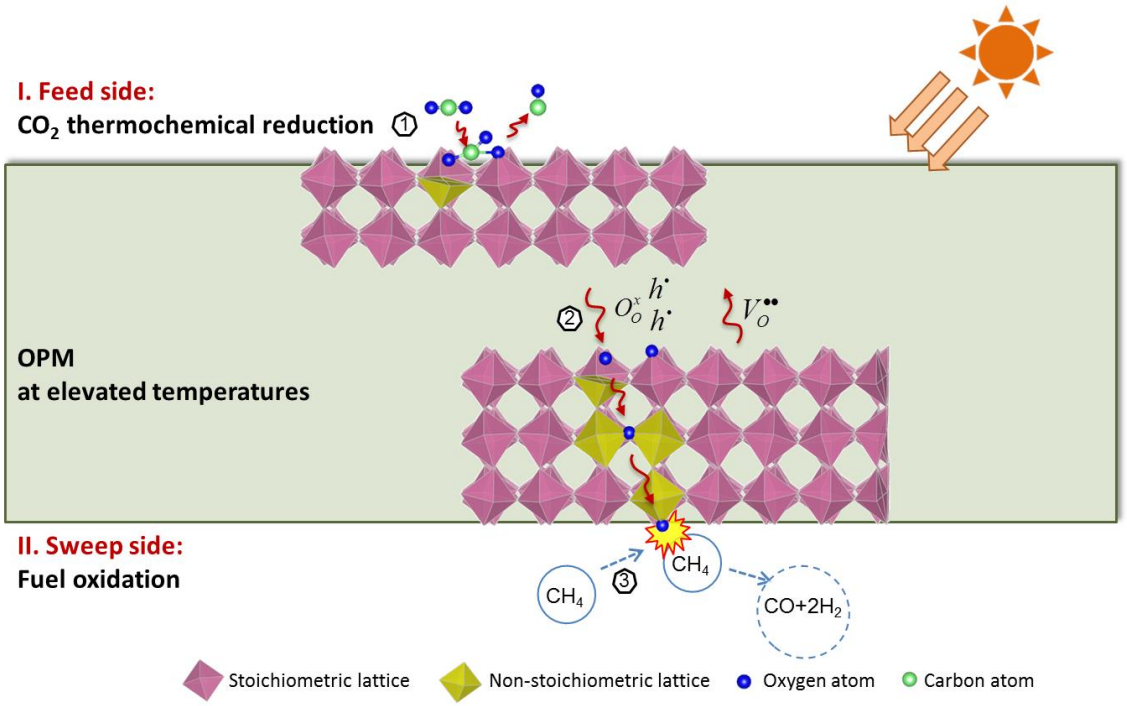

Figure 1 A schematic plot shows the steps for CO_2 thermochemical reduction on a perovskite oxygen permeable membrane (OPM) with solar heat utilization as an example. Partial oxidation of methane is used as an example to illustrate the potential of energy storage and chemical co-production

At moderate temperatures, homogeneous CO_2 thermal dissociation kinetics in gas phase is slow and has a low equilibrium constant. At equilibrium, the CO concentration is 5.49 ppm at 900^{o}C. The value increases to 24.9 ppm at 1000^{o}C and 3620 ppm at 1500^{o}C [34] [35]. Although solar collector/concentrator can achieve temperatures as high as 1500^{o}C [36], high-temperature operation raises the cost, and radiation heat losses makes operating above 1000^{o}C unfavorable. Temperatures in the range of 850–1030^{o}C are desirable for this OPM reactor. In this paper, we will show that at such intermediate temperatures CO_2 reduction can be enhanced in an LCF-91

OPM reactor by shifting the thermodynamic equilibrium while catalyzing the dissociation on the surface.

2.2 Reaction mechanism

Micro-kinetic mechanisms for heterogeneous CO_2 reactions on different materials are still under development. Two possible pathways have been proposed, either an oxygen atom from CO_2 incorporating as lattice oxygen, or CO_2 forming carbonates [24]. The oxygen direct-incorporation pathway was revealed from isotope experiments on a Fe-doped $SrTiO_3$ single crystal surface at 850 – 1000°C as [37]

$$CO_2(g) \leftrightarrow CO(g) + O_{ads}^{-} + h^{\bullet} \quad (1)$$

$$O_{ads}^{-} + V_O^{\bullet\bullet} \leftrightarrow O_O^{x} + h^{\bullet} \quad (2)$$

Here Kröger–Vink notation is used. $V_O^{\bullet\bullet}$ is the lattice oxygen vacancy, O_O^x is the lattice oxygen, $h^{\bullet}$ is the electron hole, or more precisely the net charge in the lattice iron atoms, and O_{ads}^{-} is the adsorbed oxygen on the perovskite surface.

For the carbonate pathway, experiments show that carbonates are formed on various perovskites, such as Fe-doped [38] or Rh-doped [39] $SrTiO_3$ surfaces, $SrCo_{0.8}Fe_{0.2}O_{3-\delta}$ [40] and $BaCo_{0.4}Fe_{0.6-x}Zr_xO_{3-\delta}$ [41] when these materials are exposed to CO_2. Possible reactions have been proposed on a Fe-doped $SrTiO_3$ surface for the carbonate pathway [38]:

$$2CO_2 + V_O^{\bullet\bullet} + Ti''_{Ti} \rightarrow (CO_3)_O^X + Ti_{Ti}^X + CO \quad (3)$$

or

$$CO_2 + Ti''_{Ti} + O_O^X + 2h^{\bullet} \rightarrow (CO_3)_O^X + Ti_{Ti}^X \quad (4)$$

Here, Ti''_{Ti} and Ti_{Ti}^{X} are titanium cations with +2 and +4 valences, respectively. Yet the stability of the carbonate depends on the temperature and CO_2 partial pressure, and carbonates can decompose into oxides and CO_2 at lower CO_2 concentrations and higher temperatures [38] [40].

Similar mechanisms have been expected for the Ca-doped $LaFeO_3$ as an acceptor-doped perovskite. In this paper, the LCF-91 membranes operating in the temperature range of 850-1030^{o}C are examined. The Ellingham diagram [32] shows that $CaCO_3$ decomposes spontaneously when exposed to 1 atm CO_2 at temperatures higher than 850^{o}C. Later in this work, EDX and XRD also show that carbonates exist sparsely on the membrane surface. Hence, in high-temperature applications reported in this work, we consider the oxygen direct-incorporation reaction as a more important pathway. While further studies are needed to derive the micro-kinetics model, reactions (1) and (2) are combined into a single-step reaction to model the CO_2 thermochemical reduction reaction on the feed side as

$$CO_2(g) + V_O^{\bullet\bullet} \rightarrow CO(g) + O_O^X + 2h^{\bullet} \quad (5)$$

This oxygen incorporation reaction is similar with those for O_2 [31, 42-45] or H_2O [29, 30] incorporation in LCF-91 materials.

On the sweep side, the single-step Mars-van Krevelen (MvK) mechanism is used to model the fuel (i.e., CO and H_2) oxidation on the perovskite membrane, as:

CO sweep case: $CO(g) + O_O^X + 2h^{\bullet} \rightarrow CO_2(g) + V_O^{\bullet\bullet}$ (6)

H_2 sweep case: $H_2(g) + O_O^X + 2h^{\bullet} \rightarrow H_2O(g) + V_O^{\bullet\bullet}$ (7)

In this mechanism, the lattice oxygen on the sweep side is the active site for the fuel oxidation reaction, and the fuel molecules react directly from the gas phase with the lattice oxygen. This

mechanism has been proposed and verified for oxidation reactions on most doped or undoped oxides at elevated temperatures [46].

3. CO_2 reduction kinetics

Different reactive sweep gases such as CO, H_2 and hydrocarbon mixtures can be used to sustain an oxygen chemical potential gradient across the membrane and enable oxygen ion diffusion. Alternatives can be using a non-reactive sweep gas or a vacuum pump on the sweep side. Previous studies have shown the intensification of water splitting and partial oxidation of methane on an LCF-91 membrane, and confirmed that the former can be enhanced by methane partial oxidation reaction on the sweep side (the formation of syngas with H_2/CO = 2) [30]. In this study, carbon monoxide is first used as the reactive sweep gas (by construction) to quantify the oxygen transport kinetics, i.e., the forward reaction $CO_2 \rightarrow CO + 0.5O_2$ on the feed side surface and the reverse of the same reaction on the sweep side surface. The reaction kinetics for both CO_2 reduction and CO oxidation are parameterized from the experimental data and a resistance-network model that combines the effects of finite rate kinetics at the surfaces and charged species diffusion across the membrane.

3.1 Resistance-network model

Figure 2 shows the five global steps of oxygen transport through an MIEC membrane: two mass transfer steps between the gas phase and the membrane surface, two surface reaction steps and a bulk diffusion step through the membrane. These five steps can be modeled as a resistance network for the oxygen flux. In this work, we incorporate CO_2 reduction and fuel

oxidation into the resistance model and extend this resistance-network model to CO_2 as the oxygen source.

The two mass transfer resistances in the gas phase, i.e., *R*0 and *R*4 in Figure 2 depend on the geometry of the reactor, gas species, flow rates and temperatures, and they are important in modeling a membrane reactor. The flux from mass transfer in the gas phase, *J*, [mol cm^{-2} s^{-1}], can be expressed as,

$$J_j^i = h_{m,j}^i \left(C_{b,j}^i - C_{s,j}^i \right) \tag{8}$$

where h_m is mass transfer coefficient, [m s^{-1}], *C* is the concentration, [mol cm^{-3}]. The superscript *i* is either feed or sweep side. The subscript *j* stands for species *j*, and the subscripts *b* and *s* represent the gas bulk and surface properties, respectively. The mass transfer coefficient can be calculated from a Sherwood number correlation [47] and the species diffusion coefficients [48]. Experimental results show that when the total flow rate is higher than 50 sccm, the mass diffusion resistance in the gas phase can be neglected in the reactor (shown in the Supporting Information, Fig. S1), (i.e., $C_{s,j}^i \approx C_{b,j}^i$). In this paper, the total flow rates for feed and sweep gases are set to be 100 sccm, so the mass transfer resistances on both the feed and sweep sides are ignored. Moreover, given the relatively low temperatures and short residence time, gas phase kinetics are slow and the measurements from the outlets of the reactors represent the species concentration near the surface.

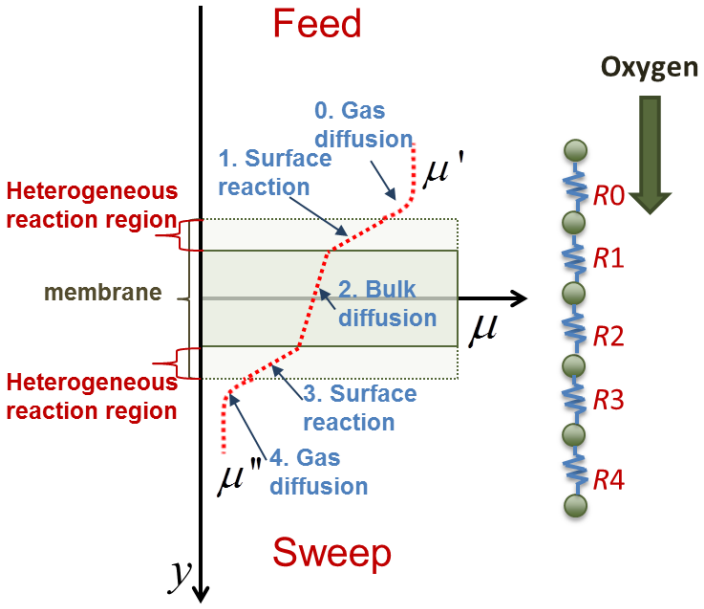

Figure 2 Resistance-network kinetic model for oxygen transport through an oxygen permeable membrane is shown. Feed and sweep sides are with high and low chemical potential, μ' and μ'', respectively. *R*i denotes the resistance corresponding to the i^{th} process on the left

Of the other three resistances, the two that involve the gas-solid reactions (i.e., *R*1 and *R*3) are parameterized as follows. As discussed previously, single-step oxygen direct-incorporation and MvK mechanisms are used on the feed and sweep sides, respectively, that is reaction (5) and (6). The "absolute" oxygen vacancy fluxes on both surfaces are

CO_2 feed side: $J'_V = k_{f,CO_2} C'_{CO_2} C'_V - k_{r,CO_2} C'_{O_O^x} C'^2_h \cdot C'_{CO}$ (9)

CO sweep side: $J''_V = k_{r,CO_2} C''_{O_O^x} C''^2_h \cdot C''_{CO} - k_{f,CO_2} C''_{CO_2} C''_V$ (10)

Here, J'_v and J''_v are the absolute values of oxygen vacancy fluxes at the feed and sweep side surfaces, respectively, [mol cm^{-2} s^{-1}]. k_{f,CO_2}, [cm^4 mol^{-1} s^{-1}] and k_{r,CO_2}, [cm^{10} mol^{-3} s^{-1}], are the reaction rate constants for reactions (5) and (6), respectively.

The oxygen vacancy diffusion flux across the membrane is driven by the chemical potential gradient $\nabla\mu_V$, [J mol^{-1} cm^{-1}]. According to the Nernst-Planck equation,

$$J_V = -\frac{\sigma_V}{\left(z_V F\right)^2}\nabla\mu_V , \qquad (11)$$

where σ_V is the conductivity of oxygen vacancy in the membrane, [S cm^{-1}], z_V is the charge of oxygen vacancy, which is taken to be +2 with respect to the ideal crystal lattice and F is Faraday constant, [s A mol^{-1}].

Several assumptions will be made to derive the permeation model:

(1) The backwards reactions on both surfaces are neglected due to the low oxygen flux compared to the total flow rate and hence, the low product concentrations compared to the reactants. Similar assumptions have been made and verified in the literature for heterogeneous reactions with MIEC membranes [49];

(2) The electron hole concentration across the membrane is assumed to be constant as the electronic transference number is much higher than ionic transference number (i.e., electronic conductivity is much higher than the ionic conductivity) [50, 51]. Therefore, the vacancy flux is viewed as zero-order in electron hole concentrations $C'^{2}_{h\bullet}$ and $C''^{2}_{h\bullet}$ [28, 52, 53]; [1]

(3) The total site concentration for oxygen species C_o (accounting for both oxygen atoms and vacancies) is

[1] In the space-charge zone near the solid-gas interface, the charged species distribution can be different. Recent studies show that the discontinuity occurs very close to the surface [54] Z. A. Feng, F. El Gabaly, X. Ye, Z.-X. Shen, W. C. Chueh, *Nature Communications* **2014**, *5*, 4374.. In this work, we assume a continuous distribution of the charged species inside the membrane.

$$C_O = C_{O_O^x} + C_V , \quad (12)$$

where $C_{O_O^x}$ and C_V are the concentrations of lattice oxygen and oxygen vacancies, respectively. C_o is assumed to have a constant value: 0.0825 mol cm^{-3}, estimated from XRD measurements of stoichiometric LCF-91 lattice size in air [55].

(4) The oxygen vacancy diffusion across a dense mixed ionic-electronic material follows the Fick's law [24, 28].

Based on these assumptions, the vacancy fluxes are simplified as:

CO_2 feed side: $$J'_V = k_{f,CO_2} C'_{CO_2} C'_V \quad (13)$$

CO sweep side: $$J''_V = \tilde{k}_{r,CO_2} \left(C_O - C''_V\right) C''_{CO} \quad (14)$$

Bulk diffusion: $$J_V = -D_V \frac{\partial C_V}{\partial y} = D_V \frac{C''_V - C'_V}{t} \quad (15)$$

Here, $\tilde{k}_{r,CO_2}$ is the new reaction constant after lumping k_{r,CO_2} and the constant electron hole concentration, [cm^4 mol^{-1} s^{-1}].

At steady state, the fluxes from equations (13), (14) and (15) are equal, and they give

$$J_V = \frac{C_O}{\frac{1}{k_{f,CO_2} C'_{CO_2}} + \frac{t}{D_V} + \frac{1}{\tilde{k}_{r,CO_2} C''_{CO}}} = \frac{C_O}{R_f + R_b + R_s} , \quad (16)$$

where R_f, R_b and R_s are the resistances of the feed side surface reaction, the bulk diffusion and the sweep side surface reaction, respectively, [s cm^{-1}] [2]. The species concentrations very close to the

[2] The term 'resistance' is defined in this work as the ratio between the flux and the driving force, and is different from the resistance due to ionic conductivity, [S cm^{-1}]. It combines material properties, ionic conductivity and the reaction rate constant, as well as the operating conditions (i.e., species concentrations).

membrane surface are calculated using Equations (24) and (25), and the kinetic parameters k_{f,CO_2} and $\tilde{k}_{r,CO_2}$ are fitted using experimental data. While more elaborate models that consider diffusion of different charge species and multi-step reactions have been developed recently [43, 45], equation (16) is sufficient to examine the role of the different resistances in the oxygen transport processes and surface chemistry, which will be discussed later in this paper.

Experiments at various operating conditions such as gas species concentrations and temperatures (shown in Table 2) were carried out to parameterize the surface reaction kinetics. Effective oxygen vacancy diffusivity is shown in Table 3, which is derived from transient dilatometry studies [31]. As is shown in Figure 3, this resistance network model for the flux fit the experimental data within ±25% error. The fitted parameters are summarized in Table 1. The activation energy values are in the same order of magnitude as those obtained using a more elaborate model (considering 4-step surface reaction mechanisms and the Poisson-Nernst-Planck diffusion) [45]. In the following, we show that the resistance-network model developed in this paper can describe the dependence of oxygen flux resulting from CO_2 thermochemical reduction on various factors.

Table 1 Reaction kinetic parameters for CO_2/CO surface reactions on LCF-91

	Parameter	A		E_a		
		Value	Unit	Value*	Ref † [45]	Unit
$CO_2 + V_O^{\bullet\bullet} \rightarrow O_O^x + 2h^\bullet + CO$	k_{f,CO_2}	1.28E15	[cm^4 mol^{-1} s^{-1}]	3.64E5	2.18E5	[J mol^{-1}]
$CO + O_O^x + 2h^\bullet \rightarrow CO_2 + V_O^{\bullet\bullet}$	k_{r,CO_2}	1.64E7	[cm^4 mol^{-1} s^{-1}]	1.57E5	0.87E5	[J mol^{-1}]

* The CO_2 thermolysis has an enthalpy change of 282.9 – 281.6 kJ mol^{-1} in the temperature range of 25 – 1000°C. The activation energy is higher to overcome the transition state

† The activation energies for the reactions with electron hole, (i.e., $Fe_{Fe}^{\bullet}$)

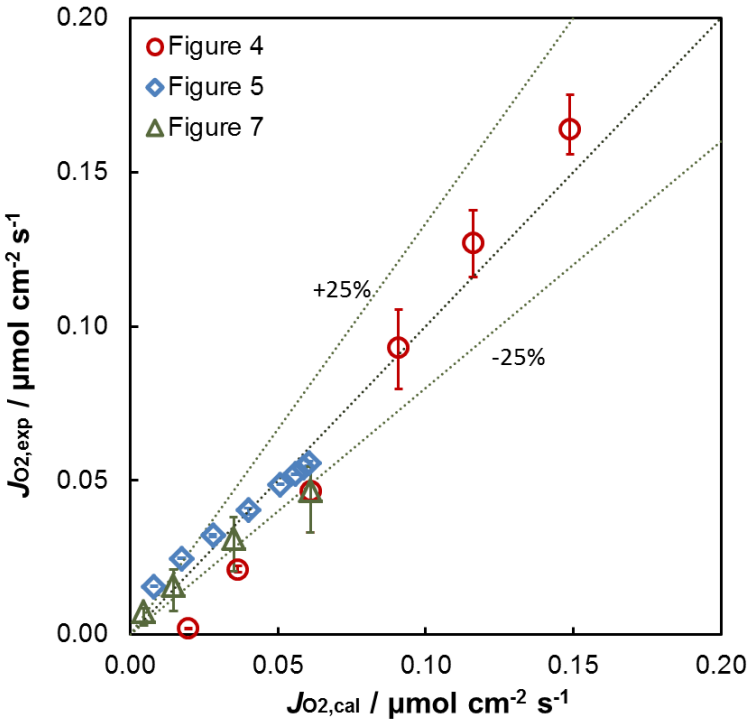

Figure 3 The oxygen flux calculated from the resistance-network model agrees well with those from experiments (The experimental data are reported later in Figures 4, 5 and 7)

3.2 Effects of fuel concentration

With argon as the sweep gas and the same total pressure (i.e., atmospheric pressure) on the sweep side, CO_2 reduction on the feed side cannot be detected by gas chromatography (GC) (within the ~10 ppm detection limit of the GC used in our experiments). This is due to the low driving force for the oxygen flux at 850-1030^{o}C. Adding 1% of CO on the sweep side, the oxygen flux increases to 0.002 μmol cm^{-2} s^{-1} as shown in Figure 4 (a). Leakage tests show there is no cross-membrane CO leak during the experiments, and hence, this is an accurate measurement of the CO_2 reduction rate (Information regarding the detection limit can be found in the Experimental Section). Further increase of fuel concentration to 11.7% on the sweep side leads to a rise of J_{O2} to 0.164 μmol cm^{-2} s^{-1}. Similar trends are observed for the CO concentration measured at the outlet on the feed side, which rises from 75.50 to 6009 ppm. Moreover, the CO concentrations at the outlet are much higher than the values corresponding to thermodynamic equilibrium (i.e., 21.7 ppm at 990^{o}C for CO_2 thermolysis $CO_2 \rightarrow CO + 0.5O_2$). An enhancement factor, F_E, [-], is defined as

$$F_E = \frac{X_{CO,outlet}}{X_{CO,equilibrium}} \tag{17}$$

The factor rises from 3.50 to 277 with increasing fuel concentration (shown in the Supporting Information, Fig. S4). This confirms that the membrane shifts the equilibrium on the feed side by in situ removal of one of the products, namely oxygen.

Figure 4 (b) shows that at low CO concentrations, the highest resistance is on the sweep side surface. However, as the fuel concentration increases, the resistances on both surfaces become of the same order of magnitude. When the fuel concentration is as low as 1%, the surface reaction resistance on the sweep side is 2×10^{6} s cm^{-1}, which is one order of magnitude higher

than the value on the feed side (i.e., 0.88 $\times 10^5$ s cm^{-1}). Yet with increasing the fuel concentration, the resistance on the sweep side drops and approaches to that on the feed side. This means both reactions on the feed and sweep sides become the rate limiting steps at high fuel concentrations. The total resistance in Figure 4 (b) also shows that at CO concentrations less than 3% on the sweep side, the total resistance drops rapidly with the fuel concentration, following the trend of the sweep side reaction resistance. Yet at higher fuel concentrations, the total resistance flattens out and shows the contribution from both feed and sweep side resistances. As a result, the slope of J_{O2} decreases as shown in Figure 4 (a). Similar trends have also been observed when water is the oxygen source that the fluxes flatten out at higher fuel concentrations [30, 56].

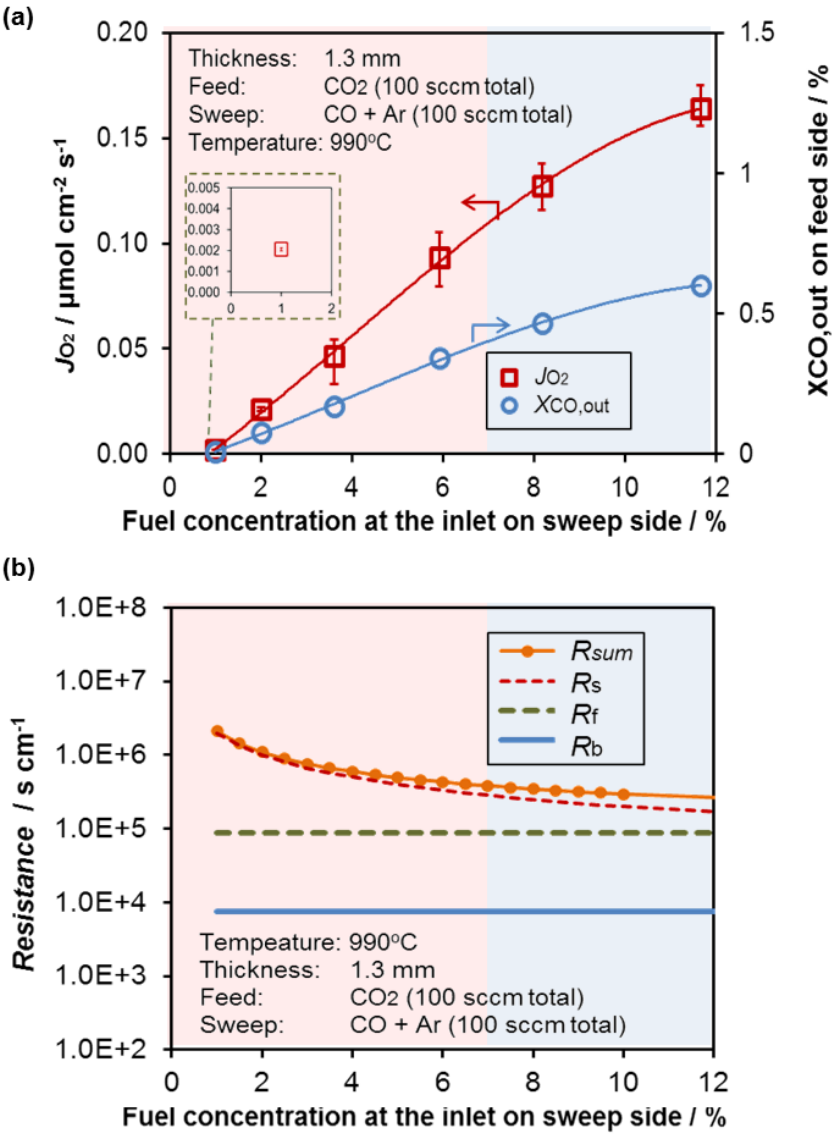

Figure 4 (a) At 990°C, the oxygen flux and CO concentration at the outlet of the feed side increase with the fuel concentration on the sweep side. The zoom-in figure shows the oxygen flux value at 1% CO at the inlet on the sweep side. (b) Resistance values are plotted under the same conditions as in (a), which shows the feed and sweep side reactions are both dominant at high fuel concentrations

3.3 Effects of CO_2 concentration

Increasing CO_2 concentration on the feed side affects the oxygen flux by accelerating the kinetics on that side. Results for a 1.3-mm thick membrane at 990^{o}C are shown in Figure 5 (a). For all cases, the concentration of CO at the inlet of the sweep side is fixed at 3.6%, which is below the transition regime associated with the fuel concentration shown in Figure 4.

With rising CO_2 concentration on the feed side, we observe two regimes for the oxygen flux. When CO_2 concentration is between 2% and 40%, the oxygen flux increases rapidly from 0.015 to 0.049 μmol cm^{-2} s^{-1}. For CO_2 above 60%, the oxygen flux asymptotes to a constant, with a 7% increase between 60% and 100%.

These two regimes can be explained by plotting the three resistances in Figure 5 (b). Since the fuel concentration is fixed on the sweep side, the resistance on that side remains constant at 6.65×10^5 s cm^{-1}. With CO_2 concentration < 10%, the feed side resistance is the highest among the three and the feed side surface reaction is the limiting step. J_{O2} rises rapidly as CO_2 concentration increases from 2 to 10%. Following that, the sweep side resistance becomes the largest, while the feed side resistance keeps decreasing with increasing CO_2 concentration. As a result, the total resistance decreases and the oxygen flux increases. With the CO_2 concentration > 60%, the sweep side resistance is more than 5 times higher than the feed side resistance, and both the total resistance (Figure 5 (b)) and the oxygen flux (Figure 5 (a)) approach this asymptotic values.

Figure 5 (a) also shows the CO_2 conversion ratio, which is defined as

$$R_{CO_2,diss} = \frac{\dot{Q}_{CO,outlet,feed}}{\dot{Q}_{CO_2,inlet,feed}}. \qquad (1\text{-}18)$$

The maximum CO_2 conversion ratio of 3% is achieved when its concentration is as low as 2% and the associated oxygen flux is 0.015 μmol cm^{-2} s^{-1}. This ratio drops continuously with increasing CO_2 concentration and it reaches 0.2% when there is 100% CO_2 on the feed side. The low values of CO_2 dissociation ratio are associated with the low oxygen flux compared to the high CO_2 feed flow rate. The O_2/CO_2 ratio is as low as 0.1 to 1.4, which is shown in the Supporting Information, Fig. S2. Depending on the dominant resistances (Figure 5), applying active catalysts for CO_2 reduction and/or for fuel oxidation, or increasing the corresponding surface area may improve the flux and the conversion ratio.

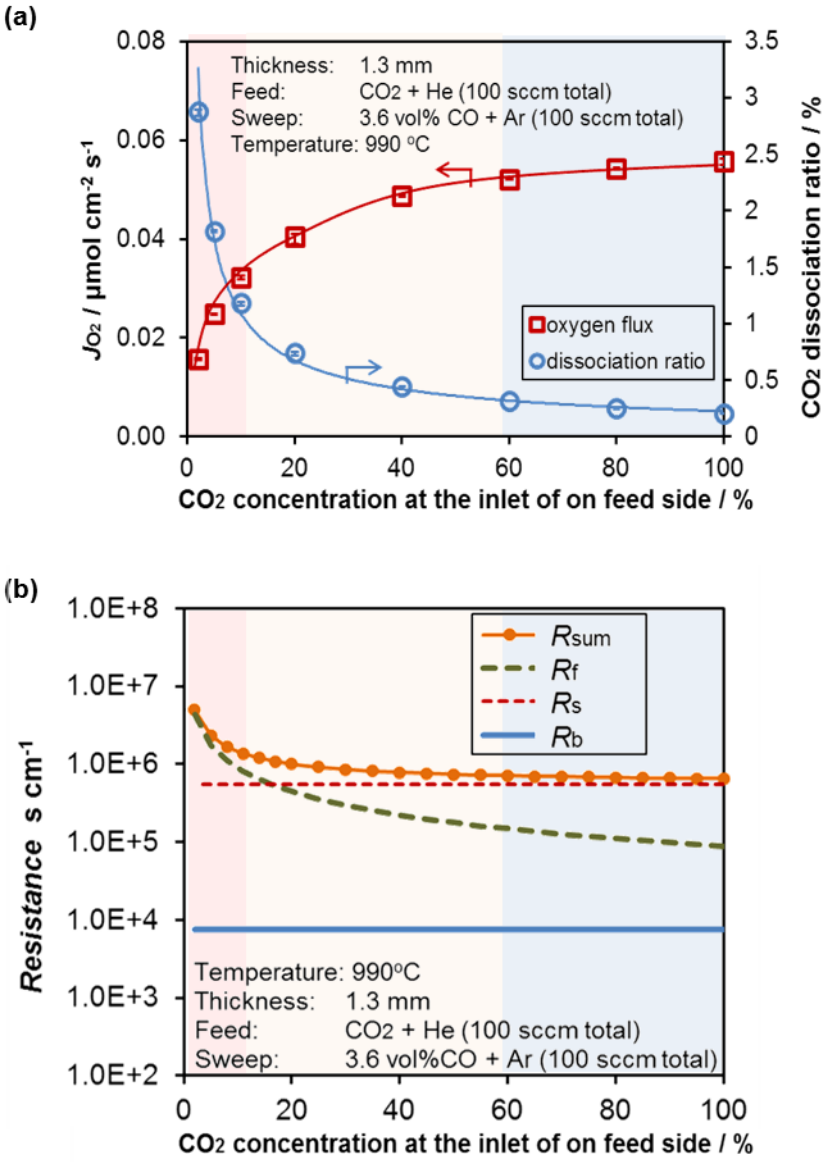

Figure 5 (a) Oxygen flux increases but the conversion ratio drops at higher CO_2 concentrations on the feed side. (b) Resistance values are plotted under the same operating conditions on (a), which shows that the dominant resistance changes from the surface reactions on the feed side to that on the sweep side when the inlet CO_2 concentration on the feed side increases

4. H_2-assisted CO_2 reduction

CO_2 reduction can be assisted by hydrogen via reverse water gas shift (RWGS) reaction [57], which favors high temperatures and is limited by thermodynamic equilibrium [58]. As the membrane reactor separates the products to overcome the equilibrium limitation, H_2-assisted CO_2 reduction in an oxygen permeation membrane reactor can facilitate the process.

4.1 Rate enhancement

H_2 oxidation has been found to be faster than CO oxidation on many oxide surfaces, such as $BaCo_{0.7}Fe_{0.2}Nb_{0.1}O_{3-\delta}$ [59], $La_{0.9}Ca_{0.1}FeO_{3-\delta}$ [45] and Ni/YSZ [60]. As the sweep side surface kinetics is the limiting step at 990^{o}C when the CO_2 concentration > 50%, adding more reactive fuel on that side is expected to improve the reduction of CO_2. The results are shown in Figure 6.

When H_2 is added in the sweep gas, the oxygen flux rises to 0.19 μmol cm^{-2} s^{-1} at 9.5% of H_2, which is about 0.04 μmol cm^{-2} s^{-1} higher than that of CO sweep under similar conditions. It is also observed that the increase rate of oxygen flux drops at higher H_2 concentrations, similar to the CO sweep case as shown in Figure 6. Under these conditions, the resistance on the hydrogen sweep side approaches the value on the feed side resistance as the fuel concentration increases. As shown in Figure 6, in the H_2 sweep case, the oxygen flux starts to flatten out at an even lower H_2 concentration (i.e., 4-6%) than that in the CO case. As H_2 reacts faster than CO on $La_{0.9}Ca_{0.1}FeO_{3-\delta}$ surfaces [45], the sweep side resistance becomes of the same order of magnitude as the feed side resistance at a lower H_2 concentration.

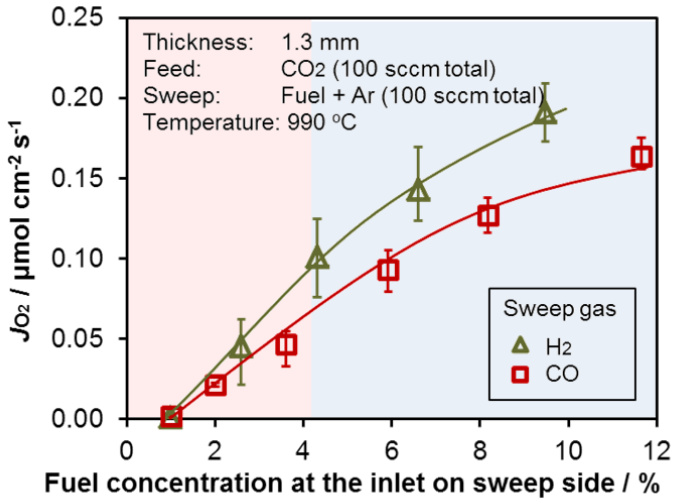

Figure 6 By increasing sweep side surface kinetics with hydrogen-argon mixture as a reactive sweep gas, the oxygen flux associated increases compared with the case of CO sweep

4.2 Temperature dependence

The dependence of the oxygen flux on the operating temperature for both H_2 and CO sweep cases is shown on an Arrhenius plot in Figure 7 (b). Pure CO_2 flows on the feed side, while 3.6% CO or 4.3% H_2 balanced with argon mixture flows on the sweep side. From this, we can see the drop in the apparent activation energy of the oxygen flux with increasing temperature for both H_2 and CO sweep cases, but at different transition temperatures.

From the resistance-network model, we know that the oxygen flux is

$$J_{O_2} = \frac{1}{2} J_V = \frac{1}{2} \frac{C_O}{R_f + R_b + R_s}. \tag{19}$$

Resistance plots are shown in Figure 7 (a) and (c) for H_2 and CO sweep cases, respectively. Both figures show that the dominant resistance is the surface reaction on either side. At low

temperatures, the feed side CO_2 reduction resistance is the highest among the three (rate-limiting), while at high temperatures the sweep side fuel (i.e., H_2 or CO) oxidation reaction resistance dominates.

As a result, oxygen flux dependence on temperature follows two regimes: at low temperatures, the barrier for the oxygen flux is dominated by the CO_2 reduction reaction on the feed side (i.e., $CO_2 + V_O^{\bullet\bullet} \rightarrow O_O^x + 2h^{\bullet} + CO$), and the oxygen flux is approximately

$$J_{O_2} \sim \frac{1}{2}\frac{C_O}{R_f}. \tag{20}$$

This reaction has an activation energy of 364 kJ mol^{-1} as shown in Table 1. At high temperatures, the activation is dominated by fuel oxidation (or perovskite reduction reaction) on the sweep side, either $H_2 + O_O^x + 2h^{\bullet} \rightarrow H_2O + V_O^{\bullet\bullet}$ or $CO + O_O^x + 2h^{\bullet} \rightarrow CO_2 + V_O^{\bullet\bullet}$. In this regime, the oxygen flux is approximately

$$J_{O_2} \sim \frac{1}{2}\frac{C_O}{R_s}. \tag{21}$$

As both reactions have lower activation energies than the CO_2 reduction reaction (shown in Table 1 and reference [45]), the apparent activation energy for oxygen transport process drops at higher temperatures.

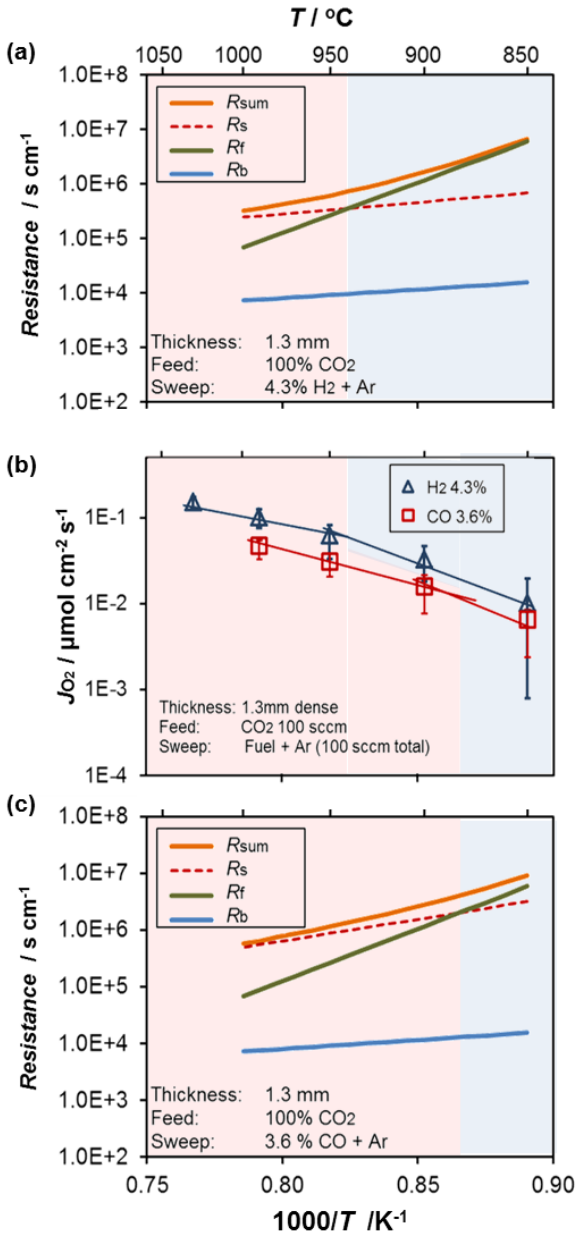

Figure 7 (a) The resistance values for the H_2 sweep case. (b) An Arrhenius plot depicting two activation energy regimes for CO_2 dissociation with 4.3% H_2 or 3.6% CO (balanced with Ar) on the sweep side on the 1.3 mm thick LCF-91 membrane, which shows that the dominant-resistance transitions between the feed and sweep side surface reactions. (c) The resistance values for CO sweep cases are plotted

Additionally, Figure 7 (b) shows that the transition temperature at which the slope changes are different for the two fuels, and the transition occurs at higher temperature when H_2 is used on the sweep side. At this transition temperature, the rate-limiting step changes in the oxygen transport process. As H_2 oxidation reaction has a faster rate constant than CO oxidation, the transition between the rate limiting steps occurs at higher temperature when H_2 is on the sweep side: around 950^{o}C in the H_2 sweep case (in Figure 7 (a)) and around 900^{o}C in the CO sweep case (in Figure 7 (c)).

5. Membrane stability

During 106 hours of CO_2 thermochemical reduction experiments under various sweep conditions and temperature (shown in Table 2), the oxygen flux remains almost constant, as is shown in Figure 8 (a). Yet the SEM, EDX and XRD analysis in Figure 8 (b) and (c) show that the membrane morphology changes, and impurities are found on the membrane surfaces following the experiments.

From the SEM images in Figure 8 (b), we see that the morphology on the feed side of the membrane changes after exposing it to 2~100% CO_2 at 850 – 1000^{o}C: irregular grains with sizes of around 1 μm appear on that surface. EDX shows calcium and iron enrichment on these irregular particles and the XRD confirms the appearance of carbonates, oxides and brownmillerite ($Ca_2Fe_2O_5$) phases forming on the feed side of the membrane. On the other hand, the sweep side surface remains clean and shows clear grain boundaries as is seen in Figure 8 (b). EDX and XRD analysis reveal that the elemental distribution and the crystal structure remain the same as before the experiments, respectively. These results show that impurities formation occurs

when the feed side is exposed to high concentration of CO_2 under the operating conditions in Table 2. Nevertheless, the impurities are located sparsely on the membrane and do not change its performance over the period of 106 hours.

Carbonate formation was found in the literature on other alkaline metal containing perovskite membranes especially on barium or strontium containing membranes such as $Ba_xSr_{1-x}Co_yFe_{1-y}O_3$ [61] and $BaCo_{1-x-y}Fe_xNb_yO_{3-\delta}$ [62] when exposed to high concentrations of CO_2. It has been found that for $BaCo_{1-x-y}Fe_xNb_yO_{3-\delta}$ membranes, the oxygen flux for air separation decreased to zero immediately when the sweep gas was switched to 100% CO_2 at 800–1000^oC, but the flux was restored when the sweep gas was switched back to an inert gas, indicating that carbonates formation is reversible and depends on temperatures and CO_2 concentrations [62]. In this work, the calcium carbonate formed on the LCF-91 membrane was less stable than barium carbonates in [62]. As a result, the performance of the LCF-91 membrane didn't degrade from carbonate formation. This confirms that the oxygen incorporation mechanism shown as reaction (5) can be an important pathway for CO_2 reduction on a LCF-91 membrane under the operating conditions in this paper.

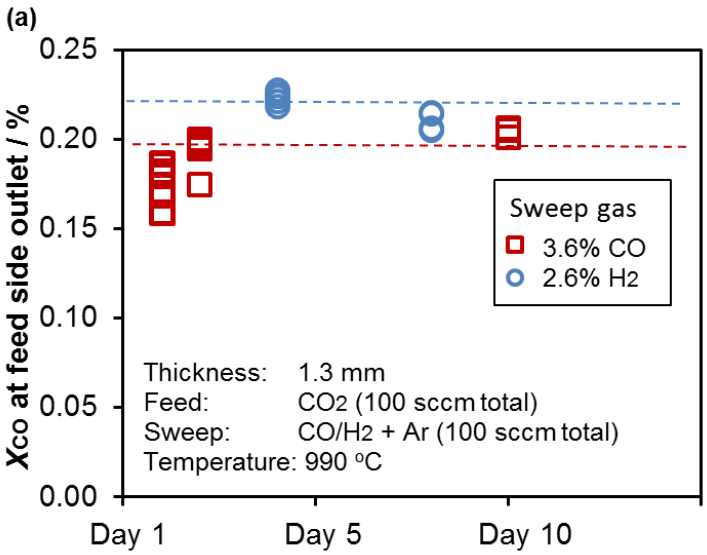

Figure 8 (a) The performances remain almost the same after 106 hours of CO_2 thermochemical reduction operation under different sweep conditions and temperatures

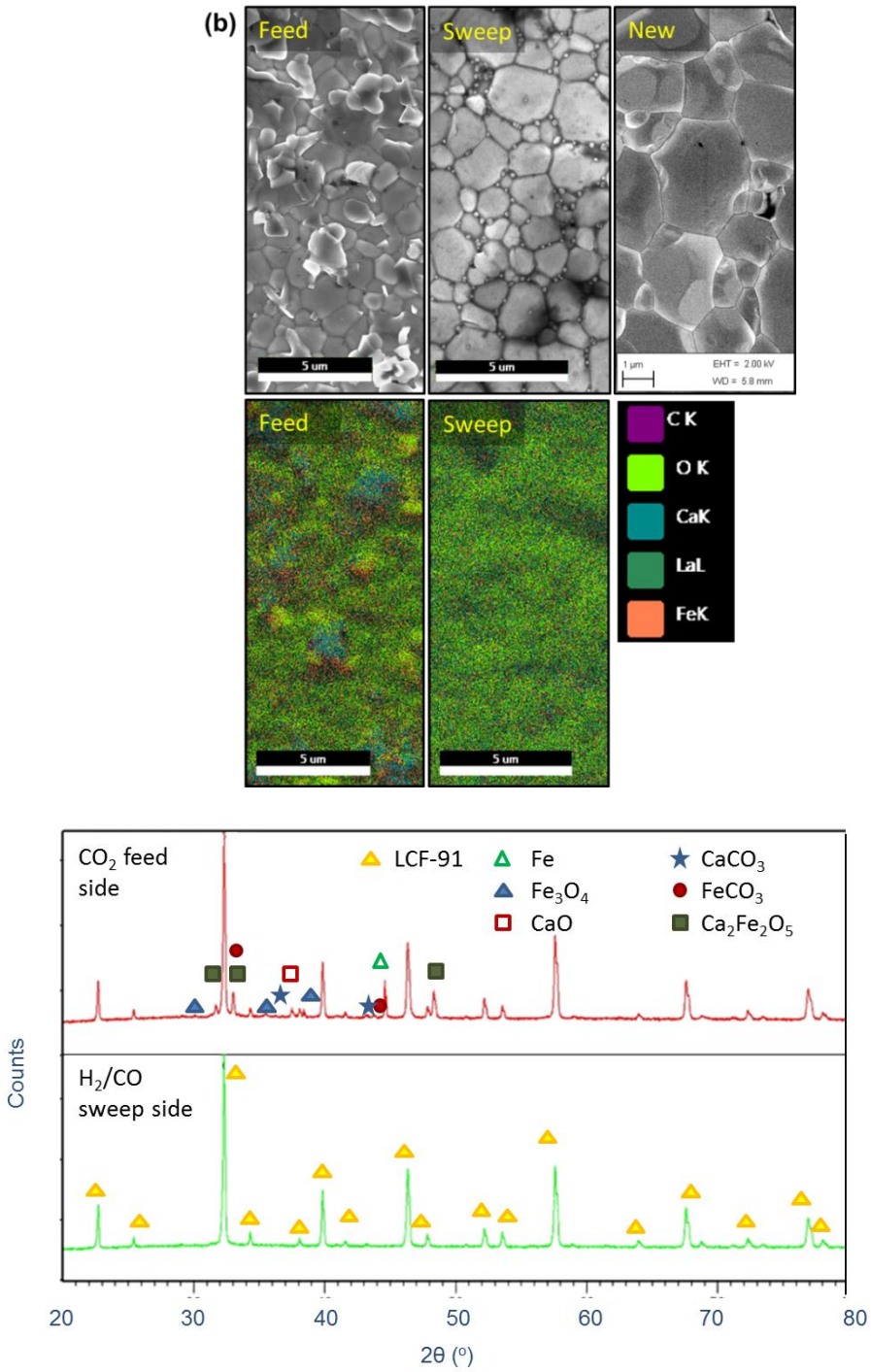

Figure 8 (b) SEM images show the morphology changes on the CO_2 feed side, and EDX analysis shows calcium and iron enrichment on the particles on that surface. (c) XRD shows the existence of impurities such as carbonates and oxides on the feed side surface

6. Conclusions

Different sources such as air and H_2O have been used to produce O_2 and/or H_2 using $La_{0.9}Ca_{0.1}FeO_{3-\delta}$ (LCF-91) membranes. In this paper, the choices of oxygen source were extended to include carbon dioxide. A model is developed to describe the oxygen transport process with CO_2 reduction and the kinetics of CO_2 reduction on the same membrane are characterized.

(1) The dependences of oxygen fluxes on the operating conditions such as the oxygen source and the fuel concentrations and temperatures were quantified. Either H_2 or CO was added into the sweep gases; the former showing better performances for assisting CO_2 reduction. The maximum oxygen flux achieved in this work was 0.19 μmol cm^{-2} s^{-1} with 9.5% H_2 on the sweep side on a 1.3 mm thick LCF-91 membrane at 990°C.

(2) A resistance-network model was developed to describe the oxygen transport process during CO_2 reduction. Kinetic parameters for CO_2/CO surface reactions on LCF-91 were parameterized using experimental data. Results show that CO_2 thermochemical reduction reaction on LCF-91 surface has higher activation energy than CO oxidation on the same material.

(3) The model also shows that in CO_2 reduction, the rate limiting step changes from the CO_2 reduction reaction on the feed side to the fuel (H_2 or CO) oxidation reaction on the sweep side at higher temperatures. This is supported by the change in the slope of the Arrhenius plot of the oxygen flux. Moreover, the transition temperature for H_2 is higher than that of CO (both used as fuels).

(4) The CO_2 reduction performances remained constant, i.e., stable performances were achieved for 106 hours of operation under different operating conditions. Following the experiment, the morphology change, impurities formation and calcium/iron enrichment were

observed on the feed side surface, while no obvious changes were found on the sweep-side surface as revealed by SEM, EDX and XRD. This supports the claim that the oxygen incorporation mechanism is an important pathway for CO_2 reduction on a LCF-91 membrane under the operating conditions in this paper.

Acknowledgment

The authors would like to thank both Shell and the King Abdullah University of Science and Technology (KAUST) for funding the research.

Experimental Section

Experimental setup

A button-cell membrane reactor with axis-symmetric reverse flow is used to study CO_2 dissociation with various reactive sweep gases. The detailed construction and use of the reactor can be found in our previous papers [29, 30]. Temperature is monitored by K-type thermocouples and controlled by a PID controller, while the gas species are examined using two gas chromatographers (i.e., 490 Micro GC and Shimadzu GC2014) with TCD detectors. The detection limit of the thermal conductivity detector is ~10ppm in our setting, and the measured CO concentration is 1-3 orders of magnitude higher than the detection limit. The gas flow rates on both sides of the membrane reactor are controlled by mass flow controllers from Brooks Instrument®. Gold sealant is used to seal the perovskite membrane to the alumina reactor chamber to endure the elevated temperatures and reactive environments. The 24 K pure gold rings are fabricated by Lux Bond & Green.

Different carrier gases on the feed and sweep sides are used to monitor the leak across the membrane during the experiments. Besides, the cases of only an inert gas on the feed side and CO-Argon mixture on the sweep side are tested every day to make sure there is no CO leakage from sweep side to the feed side.

Table 2 Operating conditions in our experiments

Temperature [^{o}C]	Feed side (dilute with He)		Sweep side (dilute with Argon)	
	CO_2 concentration	flow rate [sccm]*	fuel concentration	flow rate [sccm]
850 – 1030	2 – 100 %	100	1 – 12%	100
* The standard condition is 293.15 K and 101.325 kPa for the measurement of volumetric flow rate by the MFCs				

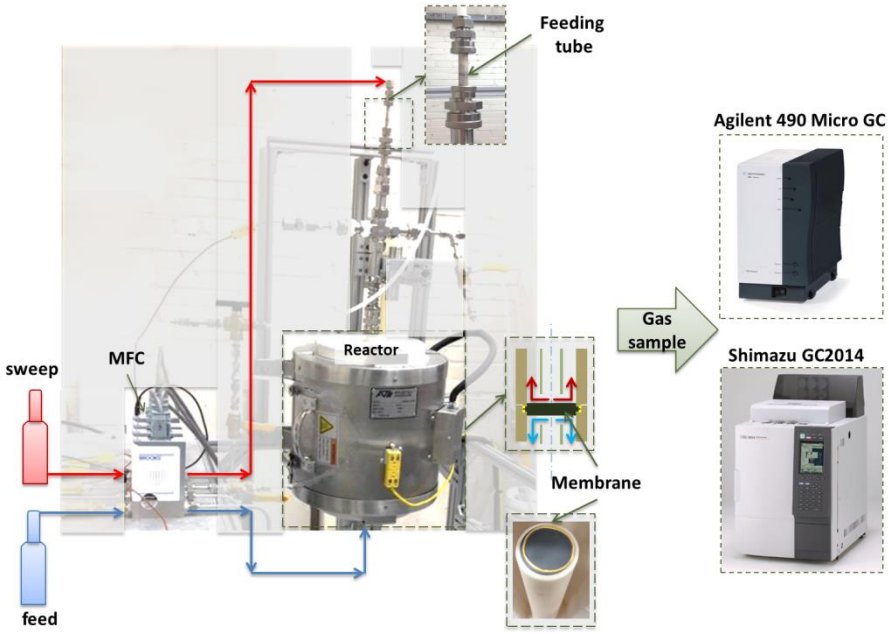

Figure 9 The schematic shows the test apparatus used in study. The feed and sweep sides are the high and low oxygen chemical potential sides in the membrane reactor, respectively

Membrane details

Dense $La_{0.9}Ca_{0.1}FeO_{3-\delta}$ (LCF-91) perovskite membranes with thickness of 1.3 mm and diameter of 16 mm were fabricated by Ceramatec. The effective diameter of the membrane is

12.7 cm as part of the membrane is covered with the gold sealant. The cation ratios are verified by EDX measurement, and the lattice structure is shown in our previous work [30]. The acceptor doped LCF-91 exhibits good oxygen permeability at elevated temperatures [63], and stable perovskite structure can be maintained with low Ca substitution [64]. The grain sizes of the as-fabricated membranes are in the order of magnitudes of one micron. Before CO_2 dissociation experiments, different inert gases are used on the two sides of the membrane reactors to make sure that the membrane is fracture-free.

The oxygen diffusivity for LCF-91 is derived from transient dilatometry studies [31]. The values are shown in Table 3.

Table 3 Oxygen diffusion for LCF-91 membrane [31]

Parameter	*A*		*E*a	
	Value	Unit	Value	Unit
D_v	4.98E-3	[cm^2/s]	5.96E4	[J/mol]

Characterization details

The SEM images and EDX data were obtained on Zeiss Merlin High-resolution Scanning Electron Microscope. The XRD analysis was carried out on a PANalytical X'Pert Pro Multipurpose Diffractometer with nickel filtered copper source with X'Celerator detector.

Data deduction

The CO concentration at the outlet of the feed chamber, $X'_{CO,out}$ is measured by gas chromatography, and the CO production rate from CO_2 thermochemical reduction is calculated as

$$\dot{Y}_{CO} = X'_{CO,\text{out}} \times \dot{n}' \tag{22}$$

where $\dot{Y}_{CO}$ is the yield of CO, [mol s^{-1}] and $\dot{n}'$ is total molar flow rate on the feed side, [mol s^{-1}].

As the CO_2 thermochemical reduction rate is low, we assume that all the oxygen produced diffuses through the membrane. Hence, the oxygen flux is related to the CO yield, as

$$J_{O_2} = \frac{\dot{Y}_{CO}}{2A_{memb}} \tag{23}$$

where J_{O2} is the oxygen flux, [mol cm^{-2} s^{-1}], and A_{memb} is effective membrane surface area, [cm^2].

The mass transfer resistance in the gas phase is ignored, and the species concentrations used in the resistance model in Equation (16) are calculated as:

$$C'_{CO_2} = \frac{X'_{CO_2,inlet} \cdot \dot{n}' - 2J_{O_2} \cdot A_{memb}}{\dot{n}'} \cdot \frac{P}{RT} \cdot 10^{-6} \tag{24}$$

$$C''_{CO} = \frac{X''_{CO,inlet} \cdot n'' - 2J_{O_2} \cdot A_{memb}}{n''} \cdot \frac{P}{RT} \cdot 10^{-6} \tag{25}$$

Here, the superscript ' and " are the properties on feed and sweep side of the membrane reactor, respectively. C_i is the molar concentration of species *i*, [mol cm^{-3}], X_i is the mole fraction of species *i*, [-], and *P* is pressure, [Pa], *R* is gas constant, [8.314 J K^{-1} mol^{-1}], *T* is the temperature, [K].

References

[1] The Keeling Curve. 2016; https://scripps.ucsd.edu/programs/keelingcurve/. Accessed May 20 2016.
[2] A. F. Ghoniem, *Prog. Energy Combust. Sci.* **2011**, *37*, 15-51.
[3] H. J. Freund, M. W. Roberts, *Surf. Sci. Rep.* **1996**, *25*, 225-273.
[4] M. Beller, G. Centi, L. Sun, *ChemSusChem* **2017**, *10*, 6-13.

[5] E. A. Quadrelli, G. Centi, J.-L. Duplan, S. Perathoner, *ChemSusChem* **2011**, *4*, 1194-1215.
[6] A. W. Kleij, M. North, A. Urakawa, *ChemSusChem* **2017**, *10*, 1036-1038.
[7] C. Graves, S. D. Ebbesen, M. Mogensen, K. S. Lackner, *Renewable and Sustainable Energy Reviews* **2011**, *15*, 1-23.
[8] H.-R. M. Jhong, C. E. Tornow, B. Smid, A. A. Gewirth, S. M. Lyth, P. J. A. Kenis, *ChemSusChem* **2017**, *10*, 1094-1099.
[9] S. Mulmi, H. Chen, A. Hassan, J. F. Marco, F. J. Berry, F. Sharif, P. R. Slater, E. P. L. Roberts, S. Adams, V. Thangadurai, *J. Mater. Chem. A* **2017**.
[10] E. E. Barton, D. M. Rampulla, A. B. Bocarsly, *J. Am. Chem. Soc.* **2008**, *130*, 6342-6344.
[11] F. Lin, M. Rothensteiner, I. Alxneit, J. A. van Bokhoven, A. Wokaun, *Energy Environ. Sci.* **2016**, *9*, 2400-2409.
[12] M. Belimov, D. Metzger, P. Pfeifer, *AlChE J.* **2017**, *63*, 120-129.
[13] M. Tou, R. Michalsky, A. Steinfeld, *Joule* **2017**.
[14] P. W. N. M. van Leeuwen, Z. Freixa, in *Activation of Small Molecules*, Wiley-VCH Verlag GmbH & Co. KGaA, **2006**, pp. 319-356.
[15] P. Furler, J. R. Scheffe, A. Steinfeld, *Energy Environ. Sci.* **2012**, *5*, 6098-6103.
[16] F. M. Jin, X. Zeng, J. K. Liu, Y. J. Jin, L. Y. Wang, H. Zhong, G. D. Yao, Z. B. Huo, *Scientific Reports* **2014**, *4*.
[17] M. E. Gálvez, R. Jacot, J. Scheffe, T. Cooper, G. Patzke, A. Steinfeld, *PCCP* **2015**, *17*, 6629-6634.
[18] L. J. Venstrom, R. M. De Smith, Y. Hao, S. M. Haile, J. H. Davidson, *Energy & Fuels* **2014**, *28*, 2732-2742.
[19] C. L. Muhich, B. W. Evanko, K. C. Weston, P. Lichty, X. Liang, J. Martinek, C. B. Musgrave, A. W. Weimer, *Science* **2013**, *341*, 540-542.
[20] M. Ezbiri, M. Takacs, B. Stolz, J. Lungthok, A. Steinfeld, R. Michalsky, *J. Mater. Chem. A* **2017**, *5*, 15105-15115.
[21] Z. Zhao, M. Uddi, N. Tsvetkov, B. Yildiz, A. F. Ghoniem, *The Journal of Physical Chemistry C* **2016**, *120*, 16271 - 16289.
[22] Z. Zhao, M. Uddi, N. Tsvetkov, B. Yildiz, A. F. Ghoniem, *The Journal of Physical Chemistry C* **2017**, *121*, 11055-11068.
[23] N. Itoh, M. A. Sanchez, W.-C. Xu, K. Haraya, M. Hongo, *J. Membr. Sci.* **1993**, *77*, 245-253.
[24] J. Sunarso, S. Baumann, J. M. Serra, W. A. Meulenberg, S. Liu, Y. S. Lin, J. C. Diniz da Costa, *J. Membr. Sci.* **2008**, *320*, 13-41.
[25] K. Zhang, G. Zhang, Z. Liu, J. Zhu, N. Zhu, W. Jin, *J. Membr. Sci.* **2014**, *471*, 9-15.
[26] R. Michalsky, D. Neuhaus, A. Steinfeld, *Energy Technology* **2015**, *3*, 784-789.
[27] K. Zhang, L. Liu, J. Sunarso, H. Yu, V. Pareek, S. Liu, *Energy & Fuels* **2013**, *28*, 349-355.
[28] S. J. Xu, W. J. Thomson, *Chem. Eng. Sci.* **1999**, *54*, 3839-3850.
[29] X. Y. Wu, L. Chang, M. Uddi, P. Kirchen, A. F. Ghoniem, *PCCP* **2015**, *17*, 10093-10107.
[30] X. Y. Wu, A. F. Ghoniem, M. Uddi, *AlChE J.* **2016**, *62*, 4427-4435.
[31] A. Hunt, G. Dimitrakopoulos, P. Kirchen, A. F. Ghoniem, *J. Membr. Sci.* **2014**, *468*, 62-72.
[32] K. Efimov, T. Klande, N. Juditzki, A. Feldhoff, *J. Membr. Sci.* **2012**, *389*, 205-215.

[33] A. Chroneos, B. Yildiz, A. Tarancon, D. Parfitt, J. A. Kilner, *Energy Environ. Sci.* **2011**, *4*, 2774-2789.
[34] D. G. Goodwin. Cantera. http://www.aresinstitute.org/Cantera/cantera-cxx.pdf. Accessed March 30 2017.
[35] G. P. Smith, D. M. Golden, M. Frenklach, N. W. Moriarty, B. Eiteneer, M. Goldenberg, C. T. Bowman, R. K. Hanson, S. Song, W. C. Gardiner, V. V. Lissianski, Z. Qin. GRI-Mech 3.0. http://www.me.berkeley.edu/gri_mech/. Accessed March 30 2017.
[36] H. L. Zhang, J. Baeyens, J. Degrève, G. Cacères, *Renewable and Sustainable Energy Reviews* **2013**, *22*, 466-481.
[37] C. Argirusis, F. Voigts, P. Datta, J. Grosse-Brauckmann, W. Maus-Friedrichs, *PCCP* **2009**, *11*, 3152-3157.
[38] F. Voigts, C. Argirusis, W. Maus-Friedrichs, *Surf. Interface Anal.* **2012**, *44*, 301-307.
[39] Q. Wu, J. Cen, K. R. Goodman, M. G. White, G. Ramakrishnan, A. Orlov, *ChemSusChem* **2016**, *9*, 1889-1897.
[40] W. Chen, C.-s. Chen, H. J. M. Bouwmeester, A. Nijmeijer, L. Winnubst, *J. Membr. Sci.* **2014**, *463*, 166-172.
[41] J. Tong, W. Yang, B. Zhu, R. Cai, *J. Membr. Sci.* **2002**, *203*, 175-189.
[42] A. Hunt, G. Dimitrakopoulos, A. F. Ghoniem, *J. Membr. Sci.* **2015**, *489*, 248-257.
[43] G. Dimitrakopoulos, A. F. Ghoniem, *J. Membr. Sci.* **2016**, *510*, 209-219.
[44] G. Dimitrakopoulos, A. F. Ghoniem, *Proceedings of the Combustion Institute* **2017**, *36*, 4347-4354.
[45] G. Dimitrakopoulos, A. F. Ghoniem, *J. Membr. Sci.* **2017**, *529*, 114-132.
[46] E. W. McFarland, H. Metiu, *Chem. Rev.* **2013**, *113*, 4391-4427.
[47] A. F. Mills, *Heat Transfer, 2nd ed.*, Prentice Hall, Englewood Cliffs, NJ, **1998**.
[48] E. N. Fuller, P. D. Schettler, J. C. Giddings, *Industrial & Engineering Chemistry* **1966**, *58*, 18-27.
[49] J. Hong, P. Kirchen, A. F. Ghoniem, *J. Membr. Sci.* **2013**, *445*, 96-106.
[50] F. Bidrawn, S. Lee, J. M. Vohs, R. J. Gorte, *J. Electrochem. Soc.* **2008**, *155*, B660-B665.
[51] M.-H. Hung, M. V. M. Rao, D.-S. Tsai, *Mater. Chem. Phys.* **2007**, *101*, 297-302.
[52] J. Hong, P. Kirchen, A. F. Ghoniem, *J. Membr. Sci.* **2012**, *407-408*, 71-85.
[53] L. Qiu, T. H. Lee, L. M. Liu, Y. L. Yang, A. J. Jacobson, *Solid State Ionics* **1995**, *76*, 321-329.
[54] Z. A. Feng, F. El Gabaly, X. Ye, Z.-X. Shen, W. C. Chueh, *Nature Communications* **2014**, *5*, 4374.
[55] G. Pecchi, M. G. Jiliberto, A. Buljan, E. J. Delgado, *Solid State Ionics* **2011**, *187*, 27-32.
[56] C. Y. Park, T. H. Lee, S. E. Dorris, U. Balachandran, *Int. J. Hydrogen Energy* **2010**, *35*, 4103-4110.
[57] W. Lin, K. M. Stocker, G. C. Schatz, *J. Am. Chem. Soc.* **2017**, *139*, 4663-4666.
[58] F. Bustamante, R. M. Enick, A. V. Cugini, R. P. Killmeyer, B. H. Howard, K. S. Rothenberger, M. V. Ciocco, B. D. Morreale, S. Chattopadhyay, S. Shi, *AlChE J.* **2004**, *50*, 1028-1041.
[59] P. Shen, W. Ding, Y. Zhou, S. Huang, *Appl. Surf. Sci.* **2010**, *256*, 5094-5101.
[60] V. M. Janardhanan, O. Deutschmann, *J. Power Sources* **2006**, *162*, 1192-1202.
[61] M. Arnold, H. Wang, A. Feldhoff, *J. Membr. Sci.* **2007**, *293*, 44-52.
[62] J. Yi, T. E. Weirich, M. Schroeder, *J. Membr. Sci.* **2013**, *437*, 49-56.
[63] T. C. Geary, S. B. Adler, *Solid State Ionics* **2013**, *253*, 88-93.

[64] P. M. Price, E. Rabenberg, D. Thomsen, S. T. Misture, D. P. Butt, *J. Am. Ceram. Soc.* **2014**, *97*, 2241-2248.

Supporting Information

H_2-assisted CO_2 thermochemical reduction on $La_{0.9}Ca_{0.1}FeO_{3-\delta}$ membranes: a kinetics study

Dr. Xiao-Yu Wu *, Prof. Ahmed F. Ghoniem

Department of Mechanical Engineering, Massachusetts Institute of Technology, 77 Massachusetts Avenue, Cambridge, MA 02139, USA

Email address: xywu@mit.edu (X.Y. Wu), ghoniem@mit.edu (A.F. Ghoniem)

1. Evaluation of the fitting

The fitting of the kinetics parameters is evaluated by the sum of squares due to error (SSE), which is defined as

$$SSE = \sum \left(J_{O_2,cal} - J_{O_2,\exp} \right)^2 \qquad \text{(S-1)}$$

The SEE is calculated to be 1.3162E-03 for the corresponding fitted parameters shown in Table 1. And the comparison between the calculated values based on the fitted parameters and the experimental data is shown in Figure 3.

2. Mass transfer evaluation

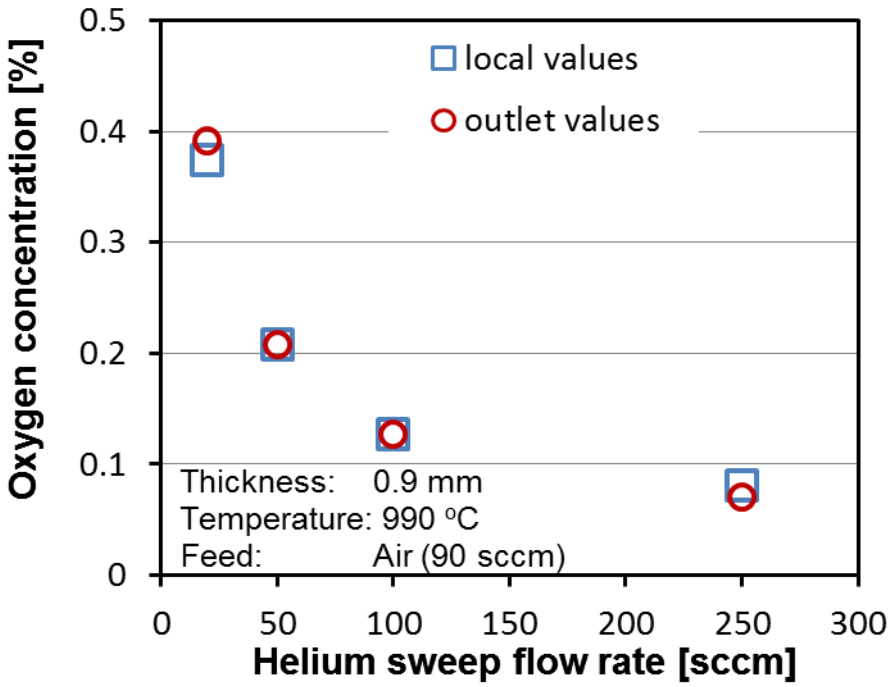

Figure S1. The comparison between oxygen concentration measurements near the membrane (local) and at the outlet with increasing sweep gas flow rate. This shows the mass transfer can be ignored when the flow rate is higher than 50 sccm, (i.e., the gas species concentrations near the membrane are close to those at the outlet).

3. Ratio of oxygen flux over the CO_2 flow rate

The ratio between the oxygen flux and the CO_2 flow rate is compared.

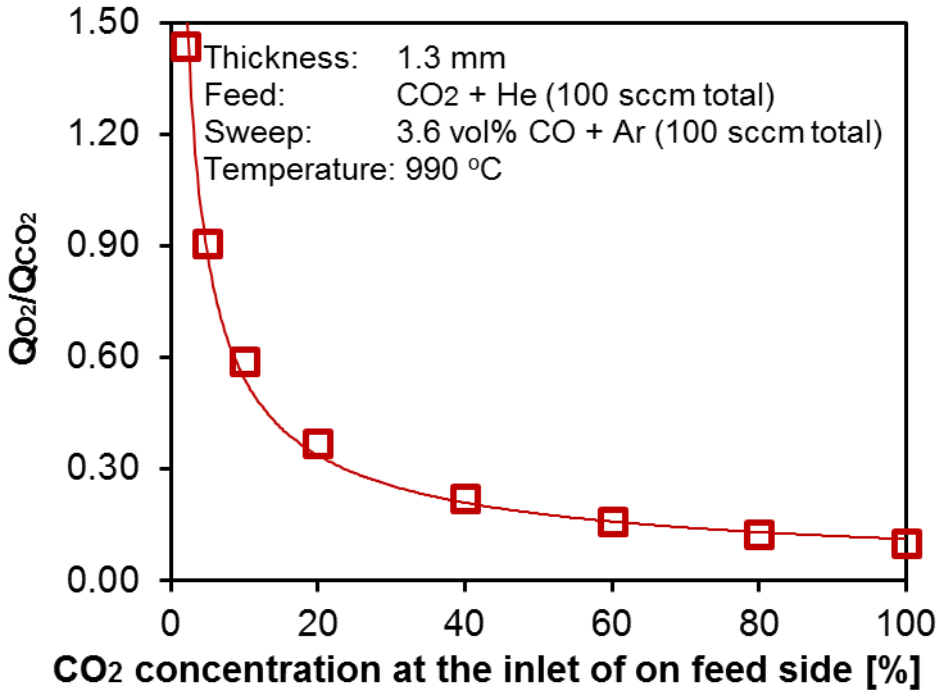

Figure S2. The ratio between the oxygen flux and the CO_2 flow rate

4. Oxygen fluxes calculated by the fitted value (H_2 sweep cases)

The oxygen fluxes are calculated using the fitted CO_2 reduction kinetics parameters (Table 1) for the cases with H_2 as the reactive sweep gas. The results show good agreement between the calculated and experimental values.

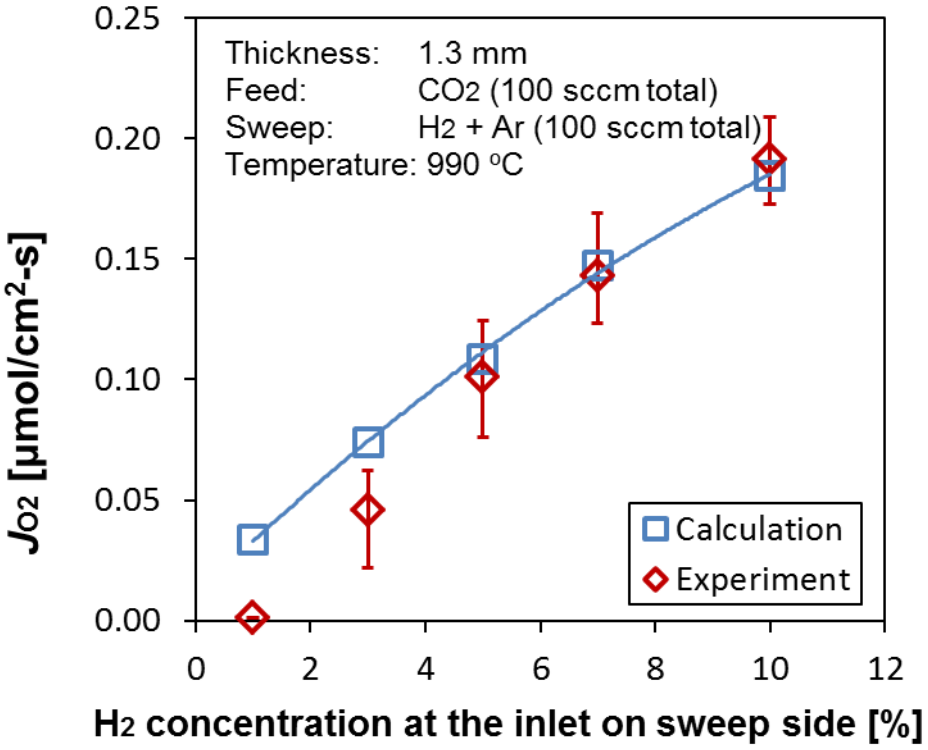

Figure S3. The comparison between the calculated values (using the CO_2/CO kinetics data fitted in this paper shown in Table 1) and the experimental values

5. Enhancement of CO_2 thermochemical reduction by the membrane

An enhancement factor, F_E, [-], is defined as

$$F_E = \frac{X_{CO,outlet}}{X_{CO,equilibrium}} \tag{S-2}$$

CO_2 thermolysis (CO_2 → $CO + 0.5O_2$) is used to calculate the equilibrium value of CO concentration.

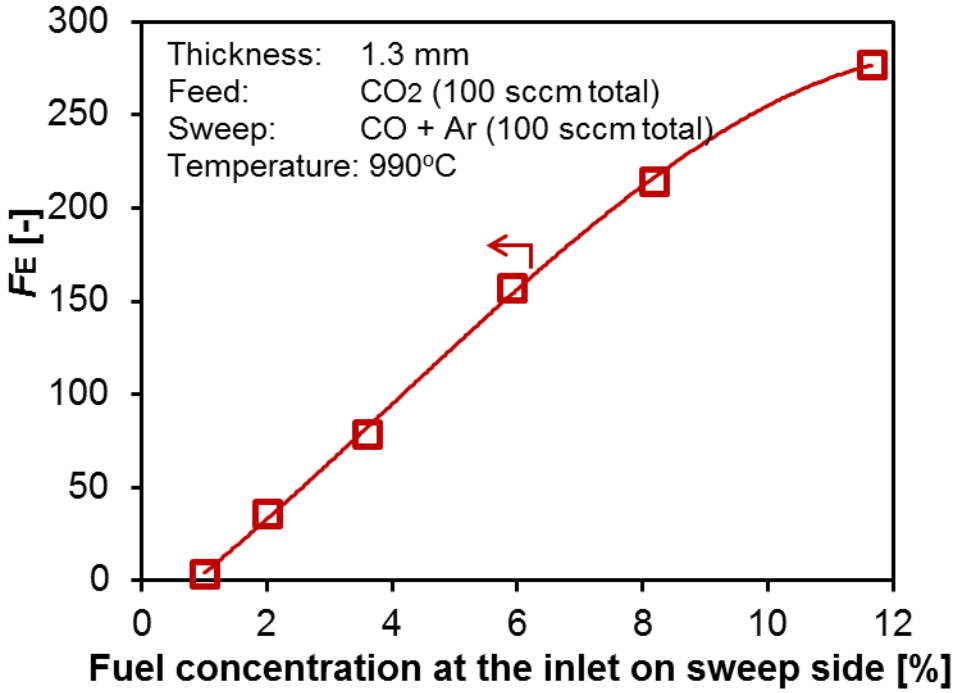

Figure S4. The enhancement factor rises from 3.5 to 277 with increasing fuel concentration on the sweep side